# Micro-structural modelling of the polarisation and properties of porous ferroelectrics

**R. W. C. Lewis, A. C. E. Dent, R.Stevens and C. R. Bowen**

[1]Materials Research Centre, Department of Mechanical Engineering, University of Bath BA2 7AY, UK
E-mail: c.r.bowen@bath.ac.uk

**Abstract.**

Micromechanical models of porous ferroelectric ceramics have often assumed that the material is fully polarised in a particular direction and/or consists of a single isolated pore. In this work the polarisation state in three-dimensional porous polycrystalline ferroelectric networks has been modelled to eradicate the oversimplification of these idealised unit cells. This work reveals that microstructural network models more closely represent a porous ferroelectric microstructure since they are able to take into account the complex polarisation distribution in the material due to the presence of high and low permittivity regions. The modelling approach enables the prediction of the distribution of poled and unpoled material within the structure. The hydrostatic figures of merits and permittivity were determined for a variety of porous lead zirconate titanate microstructures and found to be in good agreement with experimental data. The decrease in piezoelectric activity with porosity was observed to be associated with the complex polarisation state within the material. Model results were shown to be much improved when compared to a model assuming a fully-polarised model.

**Keywords:** Piezoelectric; composite; ferroelectric; polarisation

## 1. Introduction

The development of lead zirconate titanate (PZT) ferroelectric ceramics has seen the introduction and development of piezoelectric composite structures to optimise specific materials characteristics for sensor and actuator applications [1, 2]. The piezo-composite route is of interest since it is possible to tailor and optimise the mechanical stress and piezoelectric strain distribution within the material and to optimise the material performance for specific applications. Porous piezoelectrics are one example of a piezoelectric composite structure which has been considered as sensor element for low frequency hydrostatic waves, such as SONAR [3, 4], due to the improved hydrostatic figures of merit. In addition, the introduction of porosity into a polycrystalline PZT also leads to improved acoustic matching between the porous piezoelectric and other low impedance media, such as biological tissue or water [5, 6].

Porous piezoelectrics are of interest in SONAR applications since the presence of porosity decreases the transverse piezoelectric effect ($-d_{31}$) relative to the longitudinal piezoelectric effect ($d_{33}$), resulting in an increase of the hydrostatic strain coefficient ($d_h = d_{33} + 2d_{31}$). As a result of their high $d_h$, porous piezoelectric materials generate a high electrical charge per unit hydrostatic force. The introduction of porosity into PZT also decreases the permittivity at constant stress ($\varepsilon_{33}^T$), leading to an increase in $g_h$ ($= d_h/\varepsilon_{33}^T$), which is a measure of the electric field generated per unit hydrostatic stress.

To investigate the relationships between material performance and the volume fraction of porosity in a ferroelectric ceramic a number of modelling approaches have been considered [7-16]. Such models have been developed in an attempt to optimise the porous structure for particular applications. Parameters often considered are pore volume fraction [7], aspect ratio [9], shape, distribution [15] and connectivity [16]. Models consisting of a simple single pore within a polycrystalline PZT matrix have enabled the prediction of the effects of the stiffness of a passive phase, such as a polymer, within the pore and its influence on the piezoelectric

coefficients [7-14]. For the determination of piezoelectric coefficients and material permittivity, a simple single pore model is effectively dependent on the serial and parallel connection formed with respect to a porous system of PZT and air. This oversimplified model geometry can lead to poor predictions compared to experimental data, since real porous materials consist of a microstructure of many pores with a randomly distributed porosity in which some pores are connected and some isolated. With the advent of larger computational powers, more sophisticated models are achievable which can lead to the development of porous piezoelectric models [17, 18] which consist of a large number of randomly distributed pores within a polycrystalline PZT matrix.

Many of the approaches developed to date have not taken into consideration the effects of the complex electric field ($E_f$) distribution within the porous and polycrystalline ferroelectric, such as PZT. Ferroelectric materials are initially 'poled' whereby a high electric field is applied to align the ferroelectric domains in a particular direction to make the material piezoelectric. The application of an electric field to 'pole' the material is achieved by applying a potential difference between the upper and lower electrodes of the material at elevated temperature. For a dense material, with little or no porosity, the electric field is constant in both magnitude and direction throughout the material. However, for a porous PZT the presence of low permittivity porosity (relative permittivity, $\varepsilon_r=1$) in a matrix of high permittivity PZT ($\varepsilon_r > 1000$) leads to a significant variation in both the direction and magnitude of the electric field throughout the material microstructure. As a result, the poling of a porous PZT can lead to the presence of unpoled areas and poled areas with different poling directions.

This paper develops a large three-dimensional network of cells consisting of air and PZT in order to model a porous ferroelectric microstructure. The aim of the work is to provide a simple modelling methodology to understand the structure-property relationships in porous

piezoelectrics and predict transducer figures or merit. To account for variation of poling direction due the complex electric field distribution within the material the model initially examines the electric field within the porous structure to determine the distribution of polarisation directions within the composite and also identify any unpoled regions. After modelling the polarisation distribution within the porous PZT the relevant materials properties and hydrostatic figures of merit are then determined. The relevant figures of merit for 3-3 piezoelectric composites will now be described in more detail.

1.1. *Hydrostatic Figures of Merit*

The characteristics of a piezoelectric sensor can be evaluated using the hydrostatic figure of merit (HFOM) which is the product of the hydrostatic charge coefficient ($d_h$) and the piezoelectric voltage coefficient ($g_h$) [19, 20]. In SONAR applications the hydrostatic charge coefficient is used to define the hydrostatic strain per unit electric field or charge per unit hydrostatic force, and is related to the material properties parallel and transverse to the polarisation electric field direction (both $d_{31}$, $d_{32}$ transversely and $d_{33}$ parallel), as defined by Equation 1.

$$d_h = d_{33} + (d_{31} + d_{32}) \qquad \text{Equation1}$$

The piezoelectric voltage coefficient ($g_h$) is a figure of merit for a material for a hydrophone, and is defined as the electric field generated per unit hydrostatic pressure. This is calculated by the $d_h$ and the constant stress permittivity ( $\varepsilon_{33}^T$), as shown in Equation 2.

$$g_h = \frac{d_h}{\varepsilon_{33}^T} \left(\mathrm{Vm^{-1}Pa^{1-}}\right) \qquad \text{Equation 2}$$

From the product of Equations 1 and 2, the hydrostatic figure of merit may be derived ($d_h.g_h$), and is used to asses the properties of a hydrophone device in both active and passive roles [20]

## 2. Modelling methodology

A variety of analytical and finite element approaches have been developed to evaluate porous piezoceramic composites [7-16] for a number of different connectivity patterns. The over-simplification of models consisting of single pores or the assumption of a fully poled material can be overcome by the creation of a three-dimensional finite element analysis (FEA) model. The approach used in the modelling considers a large network of cells to represent a matrix of polycrystalline grains of PZT. Additional cells of air are present in the network to represent pores. The size of the model employed, 27,000 cells (i.e. a $30^3$ mesh), provides reasonable reliability and computational economy. Modification of the porosity volume fraction within the model was achieved with the ratio of assigned cells as either (i) PZT or (ii) air. Figure 1 shows and example of such a PZT-air network. Computational modelling was conducted with the finite element package ANSYS 11.0 using a coupled 8-node element (SOLID5), capable of modelling the linear piezoelectric effect. Once the 30x30x30 network of cells was constructed, two electrodes were generated by coupling the voltage degrees of freedom on the upper and lower faces of the network model.

### *2.1 Poling PZT cells*

Figure 2 shows a flow diagram of the modelling process. Initially all the PZT cells were considered to be unpoled, as in Figure 1a, and assigned the properties of unpoled PZT. An electric field was applied to the network by applying a potential difference between the upper and lower electrodes to 'pole' the material and the electric field in each of the cells examined. If the local electric field within a PZT cell ($E_f$) was less than the coercive field ($E_c$) the cell was considered to remain unpoled. If $E_f$ exceeded $E_c$ in a PZT cell it was considered to be

poled (Figure 1b). The magnitude of the coercive field is shown in Table 1. For poled cells, the polarisation direction also needs to be assigned. Shindo et al. [23] have assigned the poled properties to individual cells by rotating the piezoelectric, elastic and dielectric tensors to the new polarisation direction. We utilised a simple method that involved reading the electric field direction in x, y and z in each cell. If $E_f > E_c$, then the direction of the maximum field direction determined whether to poled cell was assigned the poled PZT properties (stiffness, piezoelectric and dielectric) in one of six potential polarisation directions; namely x, -x, y, -y, z and -z. This can be considered analogous to the six polarisation directions in the tetragonal unit cell of a ferroelectric, such as PZT [24]. Once the poled properties (and orientation) were applied to the model the piezoelectric properties of the poled porous ferroelectric could then be predicted for the network of cells for a given PZT-pore volume fraction. Domain switching can also be influenced by mechanical stress, which has not been considered in this case.

*2.2 Determination of figures of merit*

After poling the model network, the next stage was to determine the relevant material properties and figures of merit of the PZT-air network. To determine the piezoelectric strain coefficients ($d_{ij}$), a potential difference (V) was again applied to the model using the upper and lower electrodes, resulting in a strain of the network as a consequence of the piezoelectric effect in the poled PZT cells. From the resulting displacement of the network in the x, y, and z directions, the strain per unit electric field, and the $d_{33}$, $d_{31}$ and $d_{32}$ coefficients were determined. The $d_h$ parameter was then determined from Equation 1. By determining the charge (Q) developed at the model electrodes under the applied potential (V) and knowing the electrode separation (t) and area (A), the effective permittivity at constant stress $\varepsilon_{33}^{T}$ was established via Equation 3, based on the simple Q = CV relationship between charge, capacitance (C) and voltage.

Hence:-

$$Q = \frac{A.\varepsilon_r \varepsilon_{33}^{T}.V}{t} \qquad \textit{Equation 3}$$

The $g_h$ figure of merit was calculated from Equation 2, since $d_h$ and permittivity was known. The hydrostatic figure of merit was finally determined from the product $d_h.g_h$.

*2.2 Materials properties*

Table 1 and 2 show the material properties used to model the porous PZT. The properties of air ($\varepsilon_r$=1 and zero stiffness) were applied to the porosity component of the model. A commercial 'soft' piezoelectric material, PZT-5H, was chosen for this investigation for the poled PZT cells since as it is a 'soft' material typically it is used for hydrostatic sensors due to its high $d_{33}$ coefficient. Poled PZT is anisotropic and for coupled field modelling of the piezoelectric effect, the relevant properties are the stiffness matrix [$c_{ij}$], piezoelectric matrix [$e_{ij}$] and permittivity at a constant strain [$k_{ij}^{s}$]. For the six different polarisation directions the material matrices were transposed so that the 3-direction (or z-direction) in the matrix in Table 1 represented the polarisation direction (x, -x, y, -y, z or -z). The unpoled material is isotropic in terms of elastic properties and the piezoelectric coefficients, $e_{ij}$, are simply zero. The elastic properties and of the unpoled regions were determined using an equation developed by Dent [25].

It was expected that some differences would be observed between individual models at a specific pore volume fraction due to the differences in the random distribution of pores within the network. This may be particularly important for low volume fractions of PZT where the PZT cells become mechanically isolated in the network (i.e. surrounded by air cells). Similarly, at low porosity volume fractions the PZT is highly interconnected in the through-thickness direction and can be highly poled. To examine this potential variation, 50 models were developed and tested for each PZT volume fraction.

**3. Results**

The FEA modelling carried out in this work has enabled the determination of the piezoelectric coefficients, hydrostatic figures of merit and permittivity of the PZT-air biphasic composite as a function of PZT volume fraction. The influence of the complex electric field distribution during the poling process could also be examined. Figure 3 shows the predicted $d_{33}$ and $d_{31}$ as a function of PZT volume fraction. The modelling results based on the approach used in Figures 1 and 2 is termed 'Poling model' and is compared to experimental data taken from the literature [26, 27]. For a heterogeneous mixture there will be a higher intensity electric field in the low permittivity phase [28,29], and this will be particularly true in the case of a PZT-air system where the dielectric contrast ($\varepsilon_{PZT}/\varepsilon_{air}$) is in excess of 1500. Figure 4 shows the electric field magnitude in the through-thickness directions for models with 80%PZT, 50%PZT and 20%PZT. It can be seen that the air cells of lower permittivity experience a higher electric field that the high permittivity PZT cells and the electric field in the PZT begins to decrease as the PZT volume fraction decreases. To prevent dielectric breakdown within pores/defects due to the high electric field, piezoelectric composites are often polarised via 'corona' poling whereby an electric charge from a corona point is sprayed onto the sample surface creating an electric field between the sample faces. The advantage of corona poling is that a potential difference can be applied across the sample, but the absence of a conducting electrode prevents short-circuiting at such weak spots [26, 30].

To observe the influence of the polarisation process on the model output an additional set of modelling data is also shown in Figure 3 labelled 'Fully-poled model'; these results relate to the model where the PZT cells are considered to be fully poled in the same direction, an assumption in many models. It can be seen that without the poling process the $d_{33}$ coefficient for 'Fully-poled model' is almost constant as the PZT volume fraction decreases from 1 to 0.15 and there is poor agreement with experimental data. This type of model over-predicts the magnitude of the $d_{33}$ value compared to experimental data and many models of this type [7, 8, 9, 27] predict a constant $d_{33}$ with PZT volume fraction. A constant $d_{33}$ can be understood by considering a force applied to the porous piezoelectric. Since the PZT is significantly

stiffer than air, all of the force is concentrated into the PZT matrix irrespective of the PZT volume fraction; as a result the $d_{33}$ coefficient is predicted to be independent of porosity level.

At a PZT volume fraction of ~0.15 the $d_{33}$ of 'Fully poled model' falls as the PZT cells become mechanically isolated in the PZT-air network structure. For the 'Poling model' the $d_{33}$ falls gradually as porosity is introduced into the PZT phase with much improved agreement with experimental data. A comparison of the results of the 'Poling model' and 'Fully-poled model' clearly show that the gradual decrease in $d_{33}$ is due to a greater fraction of unpoled material or material poled in different orientations. The increase in the number of unpoled cells can be attributed to the poorer connectivity of the PZT cells and the concentration of electric field in the low permittivity air cells (Figure 4).

The model outputs of the transverse piezoelectric coefficient, $-d_{31}$, as a function of PZT volume fraction are also shown in Figure 3. In the range of PZT volume fractions from 0.30 to 0.95, the predicted modelled results are higher in magnitude than those of the experimental findings. The $-d_{31}$ values of the 'Poling model' are again lower in magnitude than 'Fully-poled model' as a result of the reduced degree of polarisation in the material, and are closer to the experimental data.

The high $d_{33}$ and small $-d_{31}$ values for the porous PZT lead to high $d_h$ coefficients. Figure 5 shows experimental data and modelling data for only the 'Poling model' for simplicity. Since the FEA model predicts larger $-d_{31}$ than the experimental data (Figure 3) the $d_h$ values of the model are smaller than the experimental data. Nevertheless, the general pattern of the $d_h$ rising as porosity is introduced into the PZT structure is observed in both the model and experimental results. At a PZT volume fraction 0.4 - 0.5 the $d_h$ is at a maximum since the $d_{33}$ value is still relatively large, while the $-d_{31}$ value has fallen considerably in magnitude (see Figure 3). At very low PZT volume fractions (<0.3) the value of $d_h$ begins to fall as both $d_{33}$ and $-d_{31}$ are small.

Figure 6 shows the variation in relative permittivity at constant stress ($\varepsilon^{T}_{33}$) for both models as a function of PZT volume fraction, which are again compared with experimental data. The dense material, (PZT volume fraction =1), has a high permittivity which begins to falls as porosity is introduced into the structure. The models predict a slightly higher permittivity compared to the experimental data. At a constant stress condition, the permittivity of poled PZT in greater than unpoled PZT, therefore the 'Fully-poled model' has a higher permittivity than the 'Poling model' and the agreement with experimental data is poorer. The fact that the model over-estimates both the permittivity at constant stress and piezoelectric coefficient such as $d_{31}$ indicates there may be more unpoled regions or regions poled in different directions in the real material compared to the models. This could be adjusted by the choice of coercive field or by increasing the number of potential polarisation directions.

Figure 7 and 8 show the variation of $g_h$ and $d_h.g_h$ as a function of PZT volume fraction respectively. The increase in $d_h$ (Figure 5) and the decrease in permittivity (Figure 6) leads to an increase in $g_h$ as the PZT volume fraction is reduced from unity (dense PZT) to ~0.2 (highly porous). At very low PZT volume fractions (<0.2) the $d_{33}$ (Figure 3) and $d_h$ (Figure 5) then begin to fall to small values, leading to a decrease in $g_h$. The $d_h.g_h$ follows a similar pattern with and increase in the figure of merit relative to the dense material, which a maximum figure of merit at ~0.2-0.3 PZT volume fraction. At a PZT volume fraction below 0.2, the $d_h.g_h$ decreases as the piezoelectric activity and $d_{33}$ coefficients begin to fall. Good agreement between experimental predictions and the model is observed. At a PZT volume between 0.1 and 0.4, a significant variation between the individual models at the same PZT volume fraction is observed in $g_h$ and $d_h.g_h$. This is thought to be due to PZT cells becoming isolated and dis-connected at such low PZT volume fractions.

**4. Conclusions**

The paper has described the development of a three-dimensional network consisting of a piezoelectric phase and air, to model the structure-property relationships of porous piezoelectric composites. The model includes the initial prediction of the electric field distribution in the PZT-air structure to replicate the poling process and to determine the distribution of unpoled and poled regions within the material. Comparison of the model outputs with a model that assumes a fully polarised PZT material allows the conclusion that the gradual decrease in the $d_{33}$ coefficient as porosity is introduced into the PZT matrix is primarily due to an increase in the volume fraction of unpoled regions (or regions poled in different orientations), rather than being due to a redistribution of electro-mechanical stress or strain within the structure. The evaluation of the electric field distribution and poling process enabled good agreement with experimental data which was much improved compared to a model which assumes a fully polarised model. The approach described is relatively simple and can be used to predict the piezoelectric properties of any composite structure with contrasting permittivity and/or complex electric field distributions. The micro-structural model could be improved by additional polarisation directions, rotation of the appropriate piezoelectric tensors [23], the potential influence of mechanical stress on domain switching and anisotropic pore shapes.

**References**


[1] R. E. Newnham, D. P. Skinner, K. A. Klicker, A. S. Bhalla, B. Hardiman and T. R. Gururaja, Ferroelectrics **27**, 49 (1980).

[2] J. F. Tressler, S. Alkoy and R. E. Newnham, Journal of Electroceramics **2**, 257 (1998).

[3] D. Piazza, C. Galassi, A. Barzegar, D. Damjanovic, Journal of Electroceramics **24**, 170 (2010).

[4] K. Rittenmyer, T. Shrout, W. A. Schulze and R.E. Newnham, Ferroelectrics **41**, 189 (1982).

[5] C.Galassi, Journal of the European Ceramic Society **26**, 2951 (2006).

[6] D. Piazza, C. Galassi, A. Barzegar, D. Damjanovic, Journal of Electroceramics **24**, 170 (2010).

[7] H. Banno, Japanese Journal of Applied Physics **32**, 4214 (1993).

[8] M. L. Dunn and M. Taya, J. Am. Ceram. Soc. **76**, 1697 (1993).

[9] C.R.Bowen and H.Kara, Materials Chemistry and Physics **75**, 45 (2002).

[10] H.Y. Zhang, L.X. Li and Y.P. Shen, International Journal of Engineering Science **43**, 1138 (2005).

[11] F. Levassort, M. Lethiecq, R. Desmare and L. P. Tran-Huu-Hue, IEEE Transactions on Ultrasonics, Ferroelectrics, and Frequency Control **46**, 1028 (1999).

[12] C.R. Bowen and V.Y. Topolov, Acta Materialia **51**, 965 (2003).

[13] R. Ramesh, H. Kara and C. R. Bowen, Ultrasonics **43**, 173 (2005).

[14] F. Levassort F, J. Holc, E. Ringgaard, T.Bove, M.Kose, M.Lethiecq, Journal of Electroceramics **19**, 125 (2007).

[15] R. Kar-Gupta and T.A. Venkatesh, Applied Physics Letters **91**, 062904 (2007).

[16] S. Iyer and T.A. Venkatesh, Applied Physics Letters **97**, 072904 (2010).

[17] R. W. C. Lewis, A. C. Dent and C. R. Bowen, Ferroelectrics **351**, 216 (2007).

[18] M.Asai1, N. Takano, Y. Uetsuji and K. Taki, Modelling Simul. Mater. Sci. Eng. 15, 597 (2007).

[19] H.R. Gallantree, Piezoelectric ceramic/polymer composites, Br. Ceram. Proc. **41**, 161 (1989).

[20] J. Bennett, G. Hayward, IEEE Transactions on Ultrasonics, Ferroelectrics, and Frequency Control **44**, 565 (1997).

[21] D. Berlincourt and H.A. Krueger, H.A. Properties of Morgan Electro Ceramic Ceramics. Technical Publication TP-226. Morgan Electro Ceramics (1959).

[22] M. Hooker, "Properties of PZT-based Piezoelectric Ceramics between -150 and 250 $^0$C," National Aeronautical and Space Administration (NASA), NASA/CR-1998-208708 (1998).

[23] Y.Shindo, F.Narita and M.Hirama, Smart Materials and Structures, 18, 085020, (2009)

[24]G.H. Haertling, J. Am. Ceram. Soc. **82**,797 (1999).

[25] A.C.E. Dent, "Novel Active Fibre Composites," PhD Thesis (2008), University of Bath, UK

[26] C. R. Bowen, A. Perry, A. C. F. Lewis and H. Kara, J. Euro. Ceram. Soc. **24**, 541 (2004).

[27] V. Yu. Topolov, S. V. Glushanin, and C. R. Bowen, Advances in Applied Ceramics **104**, 300 (2005).

[28] Y. Kayaba and K. Takamaro, Japanese Journal of Applied Physics, 47, 5314 (2008)

[29] S. Patil, M.Y. Koledintseva, R.W. Schwartz, Modeling of field distribution and energy storage in diphasic dielectrics, 15th IEEE International Symposium on Applications of Ferroelectrics, 310-313, 2007

[30] D.Waller, T.Iqbal, A. Safari, J.Am.Ceram.Soc. 72, 322 (1989).

**Tables.**

**Table 1.** Anisotropic material data required for modelling of materials with ANSYS 11.0. Data for PZT-5H obtained from [21], and $E_c$ at 100°C [22].

| $C_{11}^E$ (GPa) | $C_{12}^E$ (GPa) | $C_{13}^E$ (GPa) | $C_{33}^E$ (GPa) | $C_{44}^E$ (GPa) | $e_{31}$ (C/m$^2$) | $e_{33}$ (C/m$^2$) | $e_{15}$ (C/m$^2$) | $\varepsilon_{11}^s / \varepsilon_0$ | $\varepsilon_{33}^s / \varepsilon_0$ | $E_c$ (kV/cm) |
|---|---|---|---|---|---|---|---|---|---|---|
| 126 | 79.5 | 84.1 | 117 | 23.0 | -6.55 | 23.3 | 17.0 | 1700 | 1470 | 4 |

**Table 2.** Isotropic material data required for modelling of materials with ANSYS 11.0. Data for un-poled PZT-5H obtained from [25]

| Material | Density (kg m$^{-3}$) | Relative Permittivity | Young's Modulus (GPa) | Poisson Ratio |
|---|---|---|---|---|
| Un-poled PZT-5H | 7500 | 1585 | 65 | 0.37 |

**Figure Captions.**

Figure 1. (a) initial 27,000 ($30^3$) cells with a distribution of PZT and air before poling (blue regions represent unpoled PZT cells, empty regions are pores) (b) cells after 'poling' showing red poled cells.

Figure 2. Flow chart showing the approach used to model porous piezoceramic structures, taking into account the initial un-poled state and simple polarisation of the material.

Figure 3. FEA predicted $d_{33}$ and $d_{31}$ piezoelectric coefficients compared to experimental results . Experimental data from [26, 27].

Figure 4. Electric field magnitude in through-thickness direction (z) for PZT and air cells at different PZT volume fractions (a) 80% PZT, (b) 50% PZT and (c) 20%PZT. Corecive field is 0.4kV/mm and applied field based on voltage/thickness is 0.5kV/mm.

Figure 5. FEA modelling of the variation of the hydrostatic charge coefficient ($d_h$) with PZT volume fraction with $d_h$ largest at 40% PZT density. Experimental data from [26, 27].

Figure 6. Variation of relative permittivity at constant stress ($\varepsilon^T_{33}$) as a function of PZT volume fraction. Experimental data from [26, 27].

Figure 7. Variation of $g_h$ as a function of PZT volume fraction. Experimental data from [26, 27].

Figure 8. Variation of $d_h.g_h$ as a function of PZT volume fraction. Experimental data from [26,27].

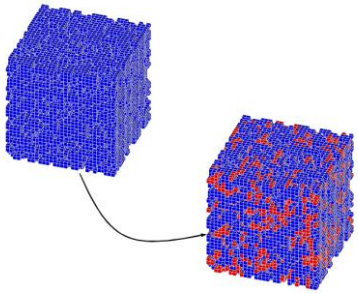

Figure 1. (a) initial 27,000 ($30^3$) cells with a distribution of PZT and air before poling (blue regions represent unpoled PZT cells, empty regions are pores) (b) cells after 'poling' showing red poled cells.

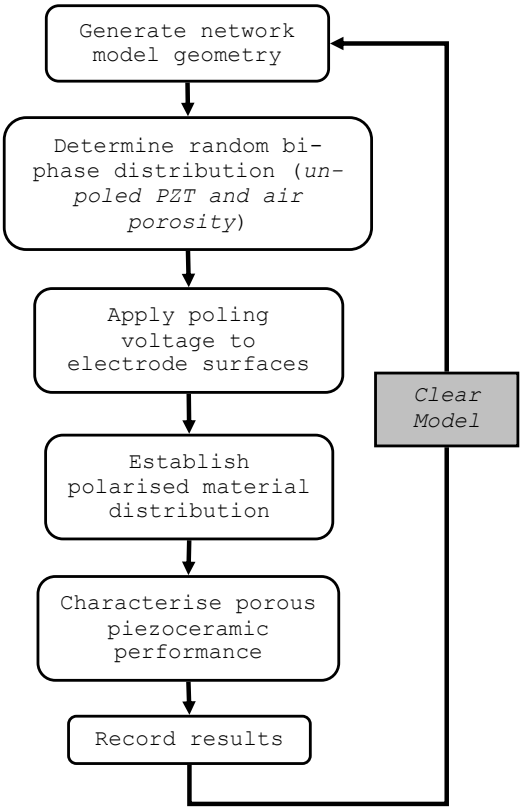


Figure 2. Flow chart showing the approach used to model porous piezoceramic structures, taking into account the initial un-poled state and simple polarisation of the material.

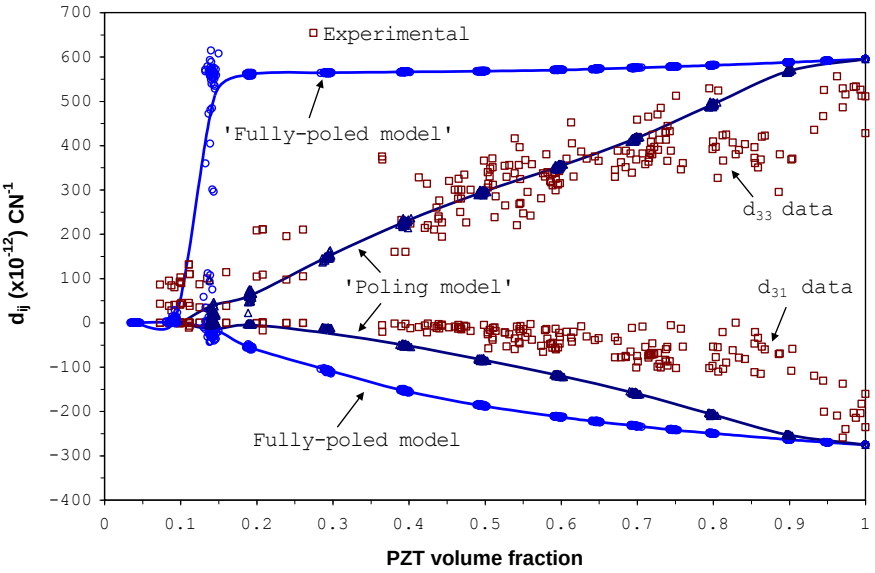


Figure 3. FEA predicted $d_{33}$ and $d_{31}$ piezoelectric coefficients compared to experimental results . Experimental data from [25,26].

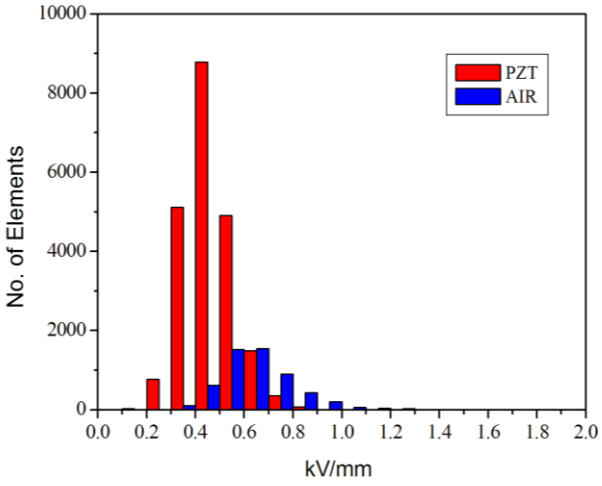


(a)

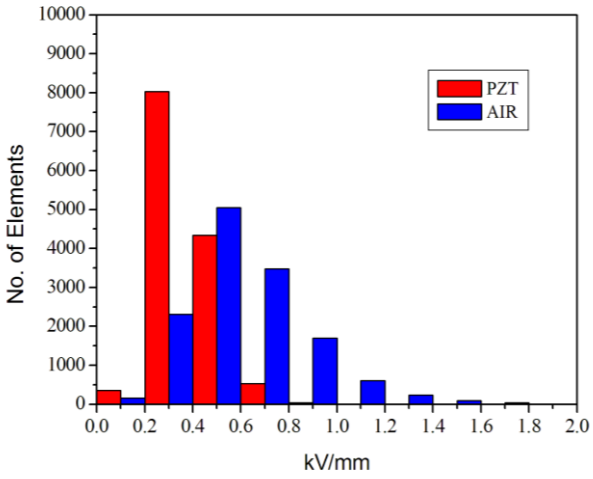


(b)

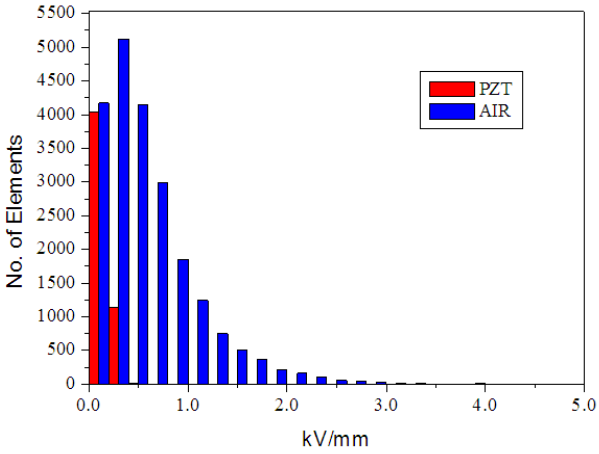


(c)

Figure 4. Electric field magnitude in through-thickness direction (z) for PZT and air cells at different PZT volume fractions (a) 80% PZT, (b) 50% PZT and (c) 20%PZT. Corecive field is 0.4kV/mm and applied field based on voltage/thickness is 0.5kV/mm.

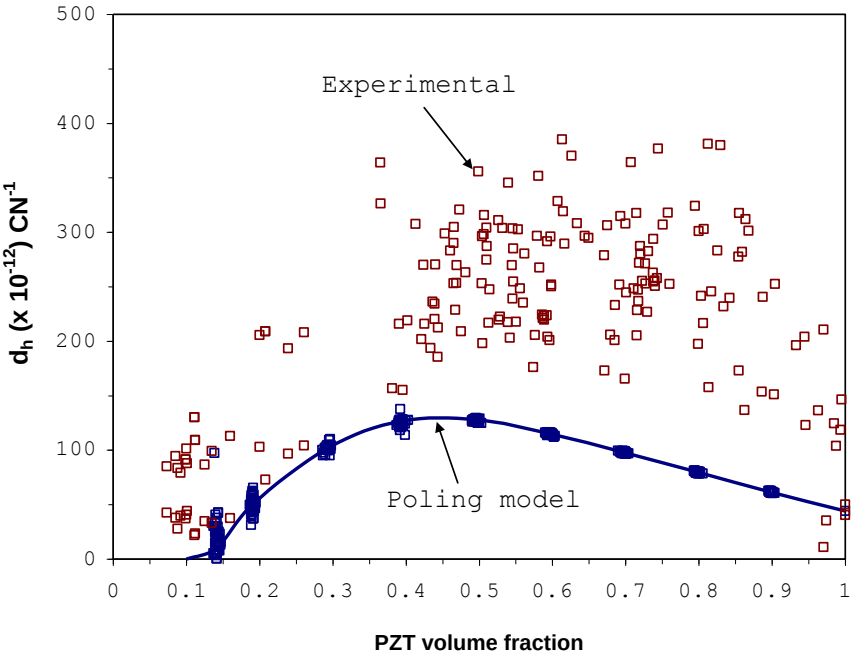


Figure 5. FEA modelling of the variation of the hydrostatic charge coefficient ($d_h$) with PZT volume fraction with $d_h$ largest at 40% PZT density. Experimental data from [25,26].

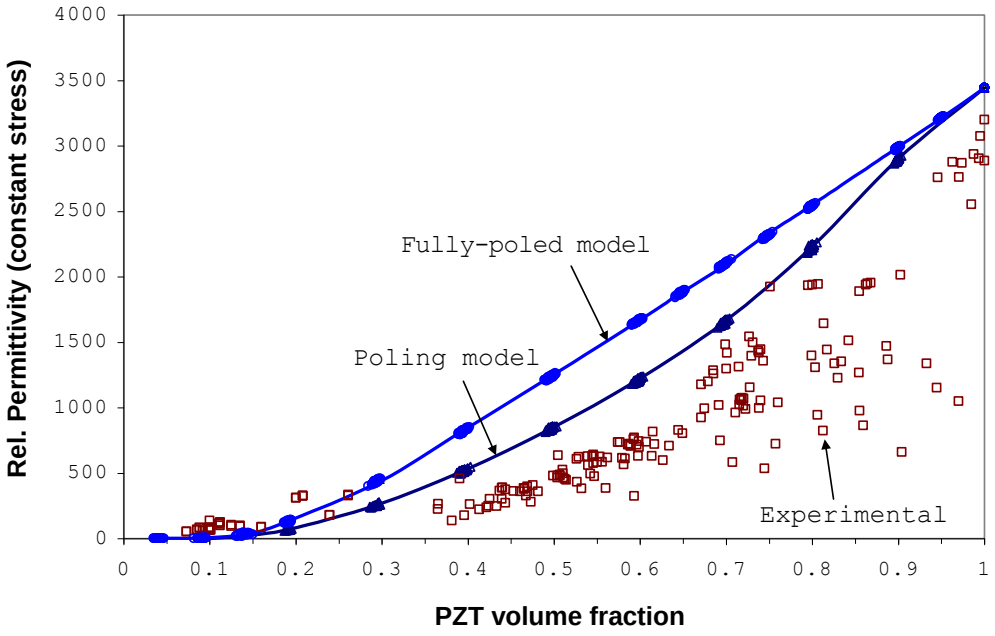


Figure 6. Variation of relative permittivity at constant stress ($\varepsilon^{T}_{33}$) as a function of PZT volume fraction. Experimental data from [25,26].

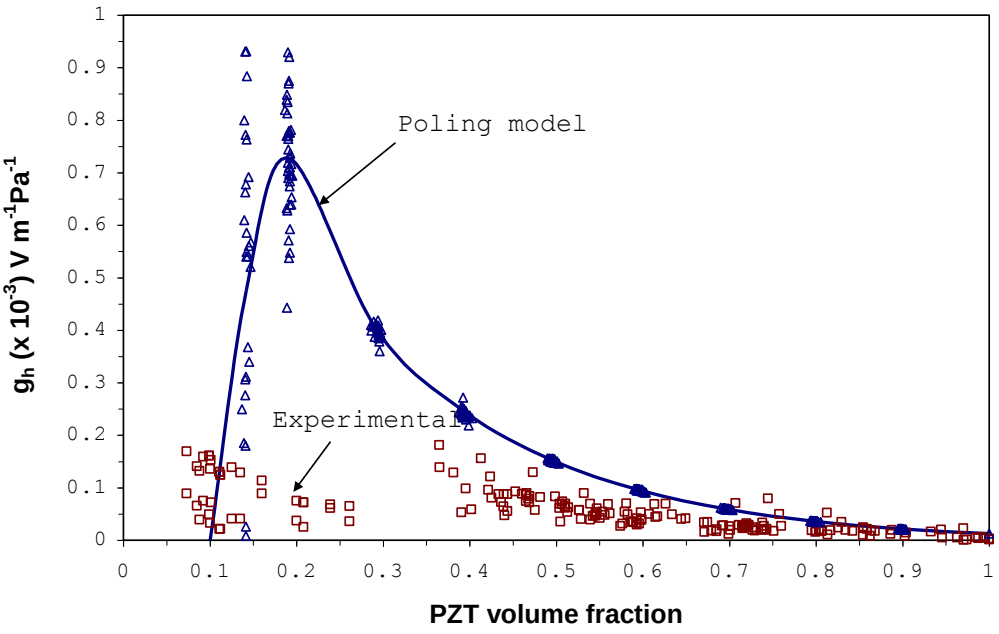


Figure 7. Variation of $g_h$ as a function of PZT volume fraction. Experimental data from [25, 26].

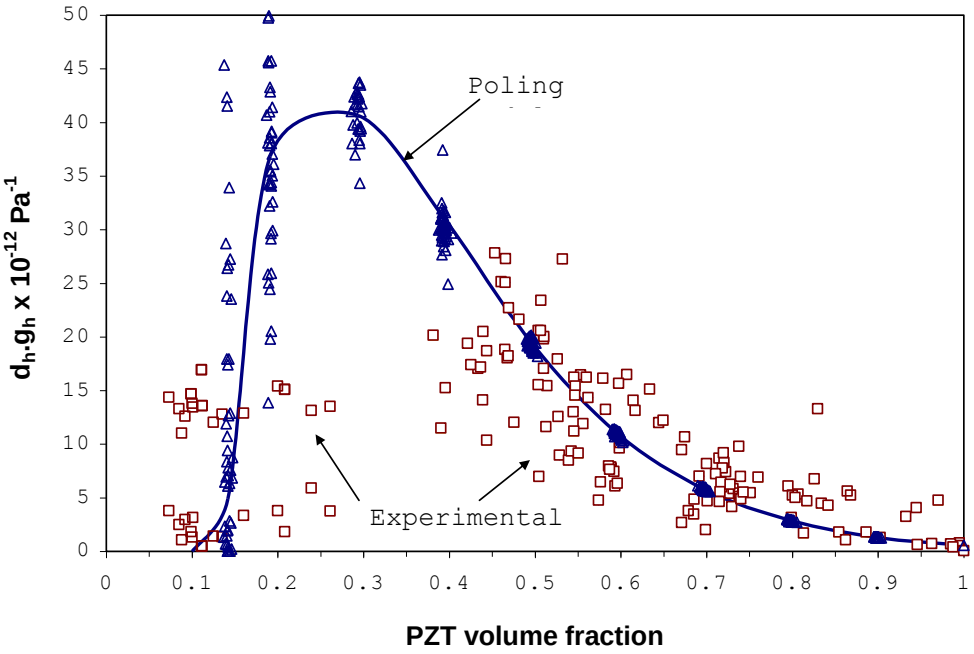


Figure 8. Variation of $d_h.g_h$ as a function of PZT volume fraction. Experimental data from